ISSN 0001-4338, Izvestiya, Atmospheric and Oceanic Physics, 2014, Vol. 50, No. 9, pp. 867–877. © Pleiades Publishing, Ltd., 2014.
Original Russian Text © R.N. Achmetov, N.R. Stratilatov, A.A. Yudakov, V.I. Vezenov, V.V. Eremeev, 2014, published in Issledovanie Zemli iz Kosmosa, 2014, No. 1, pp. 17–28.

Models of Formation and Some Algorithms of Hyperspectral Image Processing

R. N. Achmetov[a], N. R. Stratilatov[a], A. A. Yudakov[a], V. I. Vezenov[a], and V. V. Eremeev[b]

[a] *State Research and Production Space Rocket Center "TsSKB-Progress," Samara, Russia*

[b] *Ryazan State Radio Engineering University, Ryazan, Russia*

e-mail: foton@rsreu.ru

Received April 25, 2013

Abstract—Algorithms and information technologies for processing Earth hyperspectral imagery are presented. Several new approaches are discussed. Peculiar properties of processing the hyperspectral imagery, such as multifold signal-to-noise reduction, atmospheric distortions, access to spectral characteristics of every image point, and high dimensionality of data, were studied. Different measures of similarity between individual hyperspectral image points and the effect of additive uncorrelated noise on these measures were analyzed. It was shown that these measures are substantially affected by noise, and a new measure free of this disadvantage was proposed. The problem of detecting the observed scene object boundaries, based on comparing the spectral characteristics of image points, is considered. It was shown that contours are processed much better when spectral characteristics are used instead of energy brightness. A statistical approach to the correction of atmospheric distortions, which makes it possible to solve the stated problem based on analysis of a distorted image in contrast to analytical multiparametric models, was proposed. Several algorithms used to integrate spectral zonal images with data from other survey systems, which make it possible to image observed scene objects with a higher quality, are considered. Quality characteristics of hyperspectral data processing were proposed and studied.

Keywords: hyperspectral imagery, image fusion, segmentation, classification, atmospheric correction

DOI: 10.1134/S0001433814090023

INTRODUCTION

Hyperspectral imagery has been actively introduced in the Earth remote sensing in recent years (Gut, 1999; Kozoderov et al., 2012). This imagery is based on splitting radiant energy reaching the entrance pupil of the onboard observation system into several dozen and hundreds of very narrow contacting wavelength subranges. As a result, different spectral images forming the so-called hypercube are simultaneously formed:

$$B \in \left\{B_{kmn}, k = \overline{1, K}\right\}, \quad m = \overline{1, M}, \quad n = \overline{1, N},$$

where k is the spectral subrange number, (m, n) are point image coordinates (point line and column numbers), and B_{kmn} is the energy brightness at point (m, n) in the kth frequency subrange (Fig. 1). That is hypercube includes K equal images, each of which describes the emission energy of the observed object scene in a certain kth ($k = \overline{1, K}$) spectral subrange. The image in the form of the energy brightness matrix B_{kmn}, k = const, $m = \overline{1, M}$, $n = \overline{1, N}$, corresponds to a fixed k.

The K-dimensional vector of energy brightness values, which is called the spectral characteristic (SC) $B_{mn} = \left[b_{1mn}, b_{2mn}, b_{3mn}, \ldots, b_{Kmn}\right]$, m = const, n = const. corresponds to each image point with coordinates (m,n). Energy brightness can be specified as codes of imagery output signals, spectral radiance (SR), or spectral brightness coefficients (SBCs). These values can be interconverted during radiometric correction performed using data of ground or onboard calibration.

In contrast to the panchromatic and spectral zonal imagery, hyperspectral imagery represents the unique possibility of estimating the physicochemical properties of the observed scene object based on measuring SC (Pozhar and Pustovoit, 1996). If the SC is known at each hypercube point, this makes it possible to simplify substantially the segmentation and classification of the observed objects, which are the most difficultly formalized image analysis processes.

Abroad, the hyperspectral imagery method has been used to study the Earth for more than ten years (Gut, 1999; Akhmet'yanov et al., 2013). In Russia, the first attempt to install hyperspectral equipment designed by NPO Lepton was performed on the FKI small spacecraft (NPO S.A. Lavochkin, leading developer) (Khailov and Zaichko, 2013). The Resurs-P spacecraft (GNPRKTs TsSKB-Progress, leading

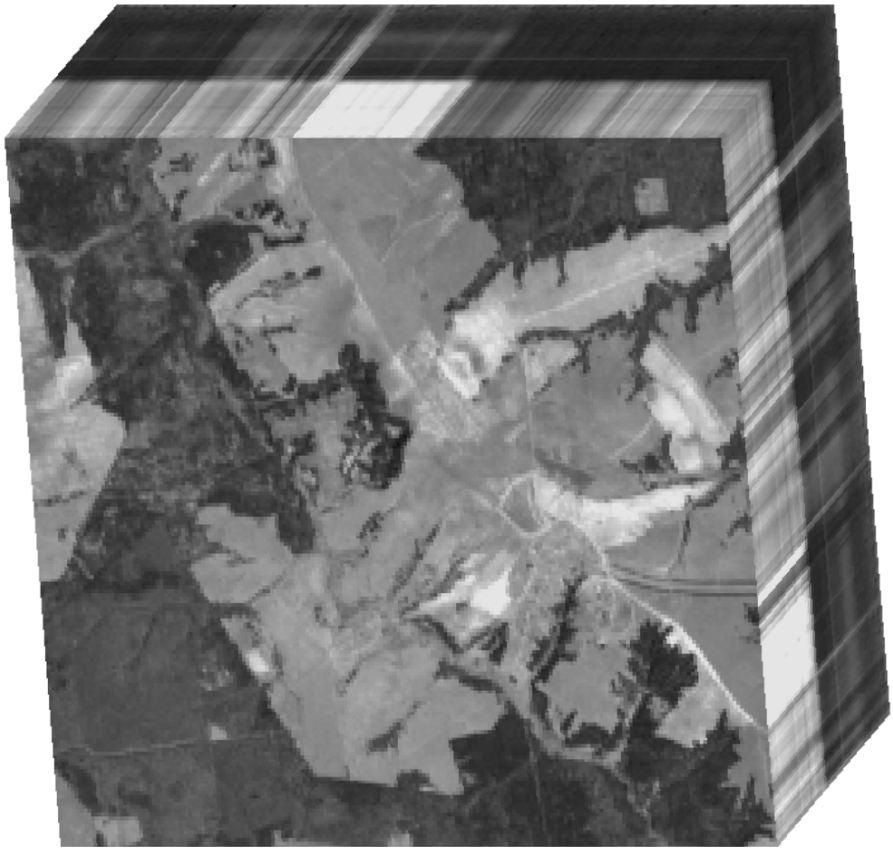

Fig. 1. A hyperspectral image: a hypercube.

developer) (Akhmetov and Stratilatov, 2011), on which hyperspectral equipment (HSE) designed at the Krasnogorsk S.A. Zverev plant (Arkhipov et al., 2013) was installed, was launched in 2013. Extensive works aimed at the creation of ground methods for processing the data from this equipment have been performed.

Hyperspectral imagery gives important information about radiant energy distribution depending on the wavelength (Bondur, 2014). At the same time, several topical issues originate when this information is processed. First, radiant energy splitting over several dozen and hundreds of channels leads to a corresponding decrease in the desired signal-to-noise ratio. This fact should be taken into account. Second, when radiant energy passes through the atmosphere, the emission spectral composition substantially changes at the entrance pupil. Therefore, this phenomenon should be strictly taken into account when the physicochemical properties of the observed objects are studied. Third, energy brightness is analyzed during the panchromatic and spectral zonal surveys; at the same time, SC objects are analyzed when hyperspectral imagery is performed. All of these specific features of hyperspectral imagery data require new approaches to their analysis and processing, which are considered in the present work.

MEASURES OF HYPERSPECTRAL IMAGE POINT SIMILARITY

Various measures of image element similarity form the basis for many segmentation, classification, and integration algorithms for different spectral data and for solving many typical problems originating when hyperspectral information is used (Bondur, 2014).

We consider three most frequently used frequency–spatial measures of similarity between two adjacent hyperspectral image (HSI) points on the line: the rms, correlation, and spectral angle measures (Yuhas et al., 1992):

$$\Delta_{mn} = \sqrt{\overline{\left(B_{mn} - B_{m+1,n}\right)^2}}, \tag{1}$$

$$\rho_{mn} = \frac{\overline{B_{mn} \cdot B}_{m+1,n} - \overline{B}_{mn} \cdot \overline{B}_{m+1,n}}{\sqrt{D_{mn} \cdot D_{m+1,n}}}, \tag{2}$$

$$\alpha_{mn} = \arccos \frac{\overline{B_{mn} \cdot B}_{m+1,n}}{\sqrt{\overline{B_{mn}^2} \cdot \overline{B_{m+1,n}^2}}}, \tag{3}$$

where D_{mn} and $D_{m+1,n}$ are dispersions of SC readings for points (m,n) and $(m+1,n)$, and a bar above the vari-

ables and expressions means averaging over the K spectral ranges, e.g., $\overline{B}_{mn} = \frac{1}{K}\sum_{k=1}^{K} B_{mnk}$.

Measure (1) characterizes the rms difference in the brightness between adjacent image elements with coordinates (m,n) and $(m+1,n)$. Measure (2) is described by the correlation coefficient between SCs determined for the same adjacent elements. Measure (3) is numerically equal to the angle in the K-dimensional spectral space. Although the proposed measures of similarity between two vectors are numerous (SCs are such vectors in our case), analysis indicates that these measures respond to the average difference squared or to the correlation, or to both parameters. In this case some functional transformations are proposed, which in any case change the behavior of these measures depending on the SC degree of closeness.

Measure (1) can be reduced to (2) by linear SC transformation (Antonushkina et al., 2010). For this purpose, we consider two hyperspectral image points (B_{mnk} and $B_{m+1,nk}$) and reduce the corresponding frequency characteristics to the unified average $\overline{B}$ and rmsd (σ) found, e.g., for the entire hypercube. We perform linear transformations B_{mnk} and $B_{m+1,nk}$, into B^*_{mnk} and $B^*_{m+1,nk}$:

$$B^*_{mnk} = a_{mn}B_{mnk} + c_{mn}, \quad B^*_{m+1,nk} = a_{m+1,n}B_{m+1,nk} + c_{m+1,n}, \tag{4}$$

where a and c are the coefficients.

We write the expressions for the average values

$$\overline{B^*_{mn}} = \overline{B} = a_{mn}\overline{B}_{mn} + c_{mn},$$
$$\overline{B^*_{m+1,n}} = \overline{B} = a_{m+1,n}\overline{B}_{m+1,n} + c_{m+1,n}$$

and rmsd

$$\sigma^*_{mn} = \sigma = a_{mn}\sigma_{mn}, \quad \sigma^*_{m+1,n} = \sigma = a_{m+1,n}\sigma_{m+1,n}.$$

With regard to these relationships,

$$a_{mn} = \sigma/\sigma_{mn}, \quad a_{m+1,n} = \sigma/\sigma_{m+1,n}, \tag{5}$$

$$c_{mn} = \overline{B} - (\sigma/\sigma_{mn})\cdot\overline{B}_{mn},$$
$$c_{m+1,n} = \overline{B} - (\sigma/\sigma_{m+1,n})\cdot\overline{B}_{m+1,n}. \tag{6}$$

Taking (5) and (6) into account, we perform transformation (4) and calculate the following measure based on obtained B^*_{mnk} and $B^*_{m+1,nk}$

$$\Delta^*_{mn} = \sqrt{\overline{\left(B^*_{mn} - B^*_{m+1,n}\right)^2}}, \tag{7}$$

where $B^*_{mnk} = (\sigma/\sigma_{mn})\cdot(B_{mnk} - \overline{B}_{mn}) + \overline{B}$, $B^*_{m+1,nk} = (\sigma/\sigma_{m+1,n})\cdot(B_{m+1,nk} - \overline{B}_{m+1,n}) + \overline{B}$.

After transformations (7) and averaging over $k = \overline{1,K}$, we obtain

$$\Delta^*_{mn} = \sigma\sqrt{2(1-\rho_{mn})}. \tag{8}$$

Expression (8) establishes the relation between two image element closeness measures: Δ^*_{mn} calculated using formula (7) and ρ_{mn} determined from (2). We can also determine the functional relation of measure (3) to measures (1) and (2) so that principal differences in the usage of any measure are absent.

An absolutely different situation is observed when HSI has additive uncorrelated noise, the level of which can be high (see above). The adequacy of such a noise model for many applications was sufficiently justified in several works (Zlobin and Eremeev, 2006). If noise ε with dispersion D_ε is present on noise images, measures (1)–(3) take the form

$$\Delta_{mn} = \sqrt{\overline{\left(\hat{B}_{mn} - \hat{B}_{m+1,n}\right)^2} + 2D_\varepsilon}, \tag{9}$$

$$\rho_{mn} = \frac{\overline{\hat{B}_{mn}\cdot\hat{B}}_{m+1,n} - \overline{\hat{B}}_{mn}\cdot\overline{\hat{B}}_{m+1,n}}{\sqrt{(D_{mn}+D_\varepsilon)\cdot\left(D_{m+1,n}+D_\varepsilon\right)}}, \tag{10}$$

$$\alpha_{mn} = \arccos\frac{\overline{\hat{B}_{mn}\cdot\hat{B}}_{m+1,n}}{\sqrt{\left(\overline{\left(\hat{B}_{mn}\right)^2} + D_\varepsilon\right)\cdot\left(\overline{\left(\hat{B}_{m+1,n}\right)^2} + D_\varepsilon\right)}}, \tag{11}$$

where $\overline{\hat{B}}_{m,n}$ and $\overline{\hat{B}}_{m+1,n}$ are SCs not distorted by noise and are averaged over all K channels.

Measures (9)–(11) are of special interest in the vicinity of the global extremums point, when $B_{mn} \approx B_{m+1,n}$:

$$\Delta_{mn} \approx \sqrt{2D_\varepsilon}, \quad \rho_{mn} \approx \left(1 + D_\varepsilon/D_{mn}\right)^{-1},$$
$$\alpha_{mn} \approx \arccos\left(1 + D_\varepsilon\Big/\overline{B^2_{mn}}\right)^{-1}.$$

It is evident that Δ_{mn} is altogether independent of the desired signal at the extremum point and completely depends on the noise level; ρ_{mn} depends on the signal-to-noise ratio; α_{mn} depends on the $D_\varepsilon\Big/\overline{B^2_{mn}}$ ratio. We introduce a new measure free of the distorting noise effect ε by modifying ρ_{mn}, having retained the previous relationship for this measure:

$$\rho_{mn} = \frac{\overline{B_{mn}\cdot B}_{m+1,n} - \overline{B}_{mn}\cdot\overline{B}_{m+1,n}}{\sqrt{\left(B_{mn}\cdot B_{m+1,n}\right)\cdot\left(B_{m+1,n}\cdot B_{m+1,n+1}\right) - \left(\overline{B}_{mn}\right)^2\cdot\left(\overline{B}_{m+1,n}\right)^2}}. \tag{12}$$

We present the examples of some operators for distinguishing contours based on measure (12).

Gradient operator: $G_{m,n} = \sqrt{\rho^2_{m+1,n} + \rho^2_{m,n+1}}$.

Laplace operator: $L_{m,n} = 0.25(\rho_{m-1,n} + \rho_{m+1,n} + \rho_{m,n-1} + \rho_{m,n+1})$.

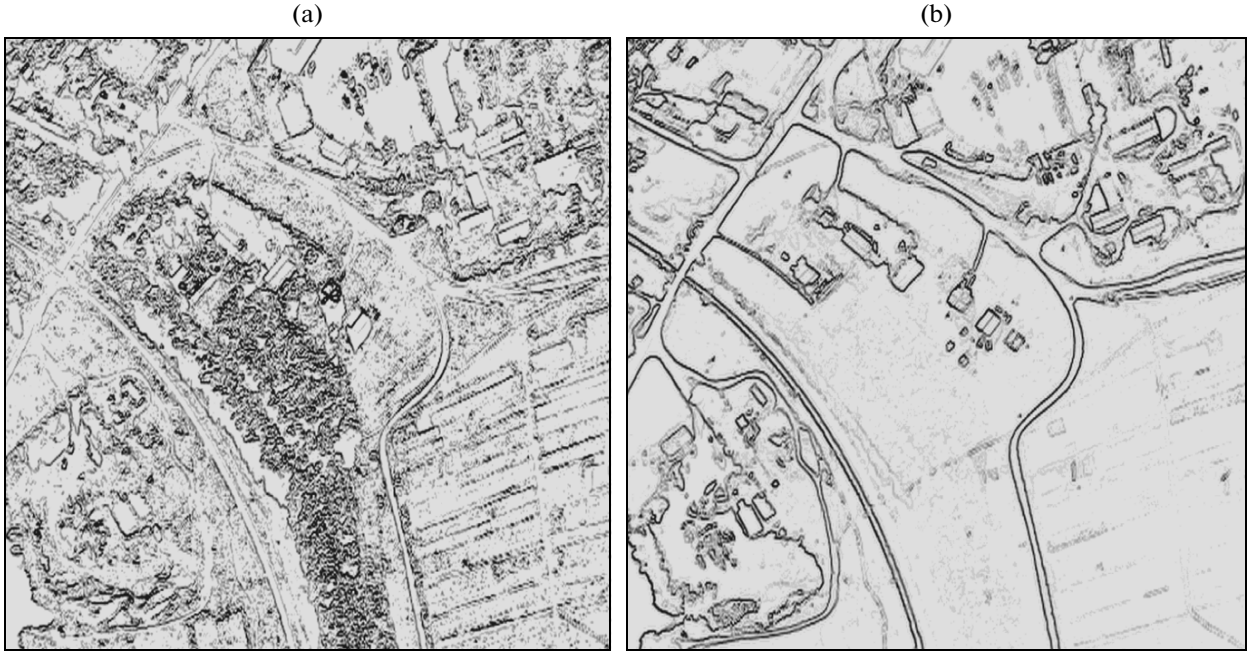

Fig. 2. Results of HSI contour processing achieved based on an analysis of (a) brightness and (b) SC.

Kirsch operator: $K_{m,n} = \min\limits_{i=0\ldots7}\left|\rho_{mn}(S_i, T_i)\right|$, dependent on variables S_i and T_i, $i = \overline{0.7}$, using the data on vector $B = \left[b_i, i = \overline{0.7}\right]$, where $b_0 = B_{m-1,n-1}$, $b_1 = B_{m,n-1}$, $b_2 = B_{m+1,n-1}$, $b_3 = B_{m-1,n}$, $b_4 = B_{m+1,n}$, $b_5 = B_{m-1,n+1}$, $b_6 = B_{m,n+1}$, and $b_7 = B_{m+1,n+1}$; $S_i = b_i + b_{i+1} + b_{i+2}$; $T_i = b_{i+3} + b_{i+4} + b_{i+5} + b_{i+6} + b_{i+7}$ (subscript i is calculated based on module 8).

Sobel operator: $S_{m,n} = \sqrt{\rho^2_{mn}(X_1, X_2) + \rho^2_{mn}(Y_1, Y_2)}$, where $X_1 = B_{m+1,n-1} + 2B_{m+1,n} + B_{m+1,n+1}$, $X_2 = B_{m-1,n-1} + 2B_{m-1,n} + B_{m-1,n+1}$, $Y_1 = B_{m-1,n-1} + 2B_{m,n-1} + B_{m+1,n-1}$, and $Y_2 = B_{m-1,n+1} + 2B_{m,n+1} + B_{m+1,n+1}$.

Thus, when HSI contours are processed, SCs of adjacent points are compared, whereas their brightness is compared in traditional algorithms.

The HSI contour processing using the gradient operator based on a brightness (Fig. 2a) and SC (Fig. 2b) analysis is illustrated in Fig. 2. It is clear that the result is higher-quality when the SC correlation gradient operator is used.

HYPERSPECTRAL INFORMATION DIMENSIONALITY REDUCTION

HSI information capacity depends on the *MNK* product; therefore, even the simplest procedures require considerable computational efforts. We studied several approaches to the reduction of the hyperspectral data redundancy, specifically, using the main component method, Wavelet transform, and SC polynomial presentation. The last approach gave slightly better results when contours were processed and objects were segmented and classified (Eremeev et al., 2012c).

The SC polynomial representation decreases the effect of additive uncorrelated noise, which is usually present on HSI. This fact follows from the approximation process, which consists in the mapping of the initial SC in the basis of K spectral channels onto the $\left\{1, i, i^2, \ldots, i^r\right\}$ basis. At $r < K$, the additive noise rmsd decreases by a factor of $\sqrt{K/r}$. Coefficients a_i, $i = \overline{0,r}$, of the polynomial approximating SC $B \in \left\{B_k, k = \overline{1,K}\right\}$ are determined using the least squares method condition $\sum_{k=1}^{K}\left(B_k - \sum_{i=0}^{r} a_i k^i\right)^2 = \min$.

After this procedure, the measure of similarity between two SCs is defined as

$$\rho = \left(\overline{P_1P_2} - \overline{P_1}\cdot\overline{P_2}\right)\Big/\sqrt{D_1D_2}, \qquad (13)$$

where $\overline{P_1P_2} = \frac{1}{K}\sum_{k=1}^{K}\left[\left(\sum_{i=0}^{r} a_i k^i\right)\left(\sum_{i=0}^{r} b_i k^i\right)\right]$, $\overline{P_1} = \frac{1}{K}\sum_{k=1}^{K}\left(\sum_{i=0}^{r} a_i k^i\right)$, $\overline{P_2} = \frac{1}{K}\sum_{k=1}^{K}\left(\sum_{i=0}^{r} b_i k^i\right)$, $D_1 = \frac{1}{K}\sum_{k=1}^{K}\left(\sum_{i=0}^{r} a_i k^i\right)^2 - \left(\overline{P_1}\right)^2$, $D_2 = \frac{1}{K}\sum_{k=1}^{K} \times \left(\sum_{i=0}^{r} b_i k^i\right) - \left(\overline{P_2}\right)^2$, and a_i and b_i, $i = \overline{0,r}$ are the coefficients of the polynomials approximating two compared SCs.

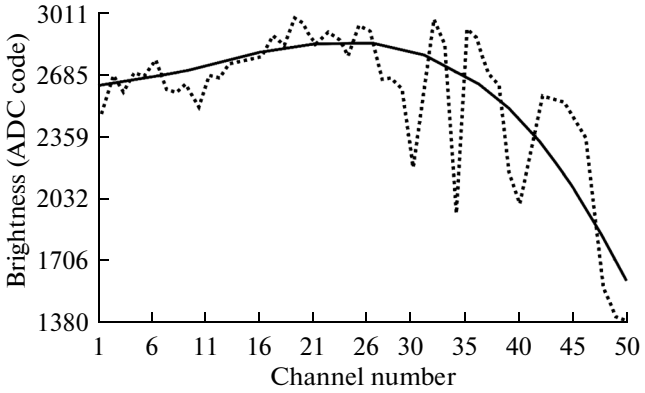

Fig. 3. Asphalt coating SC.

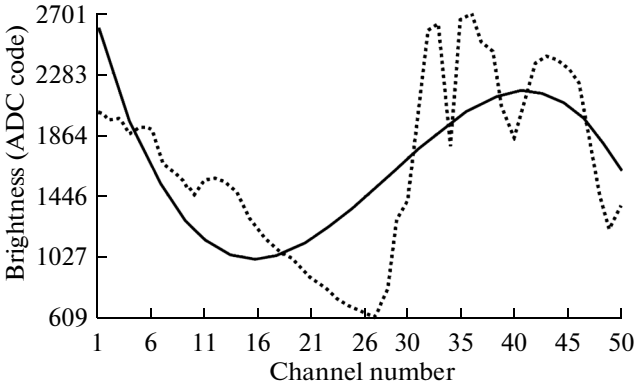

Fig. 4. Vegetation SC.

Since SC is reduced to basis $\{1, i, i^2, \ldots, i^r\}$, the computational efforts for determining (13) can be considerably decreased. We represent this expression in another form:

$$\overline{P_1} = \sum_{i=0}^{r} a_i R_i, \quad \overline{P_2} = \sum_{i=0}^{r} b_i R_i,$$

$$\overline{P_1 \cdot P_2} = \sum_{i=0}^{2r} \left[\sum_{u=0}^{r} \sum_{v=0}^{r} a_u b_v \right] R_i,$$

$$D_1 = \overline{P_1 \cdot P_1} = \sum_{i=0}^{2r} \left[\sum_{u=0}^{r} \sum_{v=0}^{r} a_u a_v \right] R_i - (\overline{P}_1)^2,$$

$$D_2 = \overline{P_2 \cdot P_2} = \sum_{i=0}^{2r} \left[\sum_{u=0}^{r} \sum_{v=0}^{r} b_u b_v \right] R_i - (\overline{P}_2)^2,$$

where $R_i = \frac{1}{K} \sum_{i=1}^{K} k^i$.

Here it is important to note that R_i can be eventually calculated beforehand and used to find K. The calculation of ρ directly requires $(3k + 6)$ multiplication and $(5k + 4)$ addition procedures. If R_i were preliminarily calculated, the ρ components are determined using r multiplications and r additions for $\overline{P_1}$ and $\overline{P_2}$, $\left(r^2 + 4r + 2\right)$ multiplications and $r(r + 2)$ additions for $\overline{P_1 \cdot P_1}$, and $\left(r^2 + 4r + 2\right)$ multiplications and $r(r + 2)$ additions for D_1 and D_2. Finally, to calculate ρ, it is necessary to perform $\left(3r^2 + 14r + 10\right)$ multiplications and $\left(3r^2 + 8r + 1\right)$ additions. For example, at $K = 100$ and $r = 3$, a direct calculation of ρ requires 306 multiplications and 504 additions; 79 multiplications and 52 additions are required when SC is represented by the polynomial of degree 3; i.e., the number of arithmetical procedures decreases by a factor of almost 4. The HSI volume decreases many times with regard to $r \ll K$, since it is necessary to conserve r coefficients for each SC at a polynomial representation.

Figures 3 and 4 present the SCs of asphalt coating and vegetation and their polynomial representation. It is clear that the polynomial representation gives SC variations (crests and depressions), which include most valuable information and are slightly affected by noise and atmospheric distortions.

The experimental studies performed using polynomial SC representations gave good results when the contours were distinguished and objects were clustered and classified.

STATISTICAL CORRECTION OF ATMOSPHERIC DISTORTIONS

The distortion action of the atmosphere causes an exclusively negative effect when HSI is analyzed and processed. Two approaches to the description and correction of atmospheric distortion exist. The first, traditional, approach (Mahiny and Turner, 2007; San, 2010) is based on multifactor analytical models, which describe radiant energy transfer from the Sun to the image sensor entrance pupil through the atmosphere. These are very complex models that require the knowledge of many parameters characterizing the state of the atmosphere and image obtaining conditions.

The second approach is based on the correction of atmospheric distortions by analyzing statistically hyperspectral imagery data (Shovengerdt, 2012). Two problem statements are possible in this case. The first, simpler, statement requires obtaining an image free of atmospheric distortions on a certain absolute energy brightness scale. Such a procedure can be used for subsequent clustering of objects on an image and their contour processing. According to the second statement, it is necessary to obtain a new image on the specific physical quantity scale, e.g., SR, which is equivalent to the usage of the analytical model of the atmosphere.

Sufficiently strict analytical models of the solar radiation passage through the atmosphere are known (e.g., Shovengerdt, 2012). Omitting the physics of this

process, we can most generally describe it as was done in (Akhmetov et al., 2013; Eremeev, 2012a; Makarenkov and Yudakov, 2012)

$$B_k(m,n) = X_k(m,n)\cdot\alpha_k(m,n) + \beta_k, \quad (14)$$

where B and X are the distorted and undistorted images; α_k and β_k are the multiplicative and additive components of atmospheric distortions. Function $\alpha_k(m,n)$ characterizes the contribution of the radiant energy that falls on the image sensor entrance pupil as a result of reflection from point (m,n) on the Earth's surface with regard to absorption in the atmosphere and topography. The additive component (β_k) describes scattered radiation from atmospheric layers that did not reach the Earth's surface but reached the image sensor input.

During satellite flight, the image lines are formed under identical conditions from the standpoint of atmospheric distortions (in the absence of clouds). In this case we can consider that $\alpha_k = \text{const}$ and $\beta_k = \text{const}$ for an arbitrary compact group of columns and estimate these coefficients using this assumption. Since atmospheric distortions change along lines, it is necessary to estimate several sets of coefficients α_k and β_k for different image columns.

We estimate brightness dispersion in each column of each hypercube spectral channel

$$D_k(m) = D\left[B_k(m)\right] = D\left[X_k(m)\cdot\alpha_k(m) + \beta_k\right], \quad k = \overline{1,K}. \quad (15)$$

Argument $m = \overline{1,M}$ in function $\alpha_k(m)$ takes into account a certain change in the solar ray propagation length from the first ($m = 1$) to the last ($m = M$) line elements, $B_k(m) = \frac{1}{N}\sum_{n=1}^{N} B_k(m,n)$. $X_k(m) = \frac{1}{N}\sum_{n=1}^{N} X_k(m,n)$.

According to the dispersion properties, expression (15) is transformed to the form

$$D_k(m) = \left[\alpha_k(m)\right]^2 D\left[X_k(m)\right]. \quad (16)$$

In such a case, we can obtain corrected element $B_k^*(m,n)$ in the following way:

$$B_k^*(m,n) = \left(B_k(m,n) - B_k(m)\right)\Big/\sqrt{D\left[B_k(m)\right]}. \quad (17)$$

Using (15)–(17), we find that $B_k^*(m,n) = \left(X_k(m,n) - X_k(m)\right)\Big/\sigma\left[X_k(m)\right]$, where $\sigma\left[X_k(m)\right]$ is the column m brightness rmsd in the hypercube kth channel.

The values obtained using expression (17) are dimensionless. Normalization to the solar radiation SR value at the upper atmospheric boundary is one of the variants of reducing these values to the physical scale:

$$\tilde{B}_k^*(m,n) = \frac{B_k^*(m,n) - \min\limits_{m,n}\left[B_k^*(m,n)\right]}{\max\limits_{m,n}\left[B_k^*(m,n)\right] - \min\limits_{m,n}\left[B_k^*(m,n)\right]} \times \left[\max(S_k) - \min(S_k)\right] + \min(S_k),$$

where $\min(S_k)$ and $\max(S_k)$ are minimal and maximal solar SR at the upper atmospheric boundary, respectively, in the wavelength range corresponding to channel k.

The considered statistical model was compared with analytical models of radiation transfer in the atmosphere (6S, RRTM) using the EO-1 Hyperion and AVIRIS (USA) data. As a result, it was established that the effect of the additive coefficient in (14) is negligible at different input data, which makes it possible to pass to the multiplicative model of the atmosphere (Akhmetov et al., 2013; Eremeev, 2012a; Makarenkov and Yudakov, 2012)

$$B_k(m,n) = X_k(m,n)\cdot\alpha_k(m). \quad (18)$$

We fix k and m in a hypercube, i.e., consider the mth column of an image in the kth spectral channel, assuming that $n = \overline{1,N}$ is variable. We obtain the average brightness value for this column

$$B_k(m) = \frac{1}{N}\sum_{n=1}^{N} B_k(m,n) = X_k(m)\cdot\alpha_k(m). \quad (19)$$

We calculate the average brightness for all mth columns of a hypercube

$$B(m) = X(m)\cdot\alpha(m), \quad m = \overline{1,M}, \quad (20)$$

where $B(m) = \frac{1}{K}\sum_{k=1}^{K} B_k(m)$, $X(m) = \frac{1}{N}\sum_{n=1}^{N} X_k(m,n)$, and $\alpha(m) = \frac{1}{K}\sum_{k=1}^{K}\alpha_k(m)$.

After this procedure, we determine corrected element $B_k(m,n)$ as

$$B_k^*(m,n) = B_k(m,n)\cdot\left[B(m)/B_k(m)\right]. \quad (21)$$

Using (18)–(20), we find that

$$B_k^*(m,n) = X_k(m,n)\cdot\left[X(m)/X_k(m)\right]\cdot\alpha(m). \quad (22)$$

In (22) $\alpha(m)$ is the constant value for all hypercube K columns with numbers m. Moreover, $\alpha(m)$ slightly depends on m, since the solar ray path length slightly varies depending on $m = 1, 2, \ldots, M$. Therefore, image readings $B_k^*(m,n)$ are proportional to undistorted $X_k(m,n)$. Applying similar considerations to all $m = \overline{1,M}$ and $k = \overline{1,K}$ values, we correct the data for the entire hypercube.

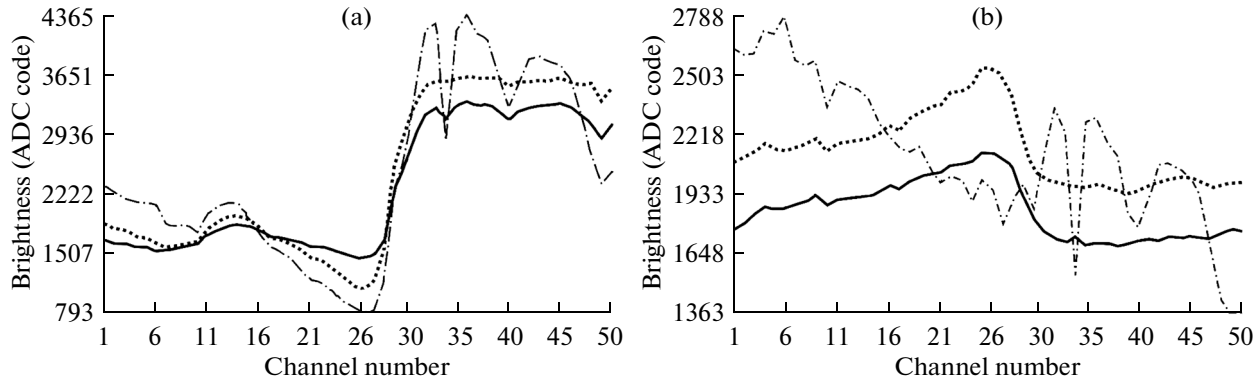

Fig. 5. SCs before and after the atmospheric correction: (a) dense vegetation, (b) open soil.

When the analytical model of the atmosphere is used, we first calculate the radiation intensity at the upper atmospheric boundary in the SR units and then take into account radiation weakening by the atmosphere on the path to the ground level. The relative values calculated using (22) can be differently coordinated with SR. This procedure is most simple when the upper and lower boundaries of the atmospheric transmission spectral characteristic at a wavelength of ~950 nm, which is caused by an abrupt radiation absorption by water vapor, are compared. We require that the upper and lower boundaries of these peaks coincide for the $B_{a,\min}$, $B_{a,\max}$ analytical model and at a statistical approach $B_{c,\min}$, $B_{c,\max}$. In such a case, it is necessary to introduce correction coefficients α_0 and β_0 in (21): $B_k^*(m,n) = B_k(m,n)\left[B(m)/B_k(m)\right]\alpha_0 + \beta_0$, where $\alpha_0 = \left(B_{a,\max} - B_{a,\min}\right)/\left(B_{c,\max} - B_{c,\min}\right)$, $\beta_0 = B_{a,\max} - B_{c,\max}\alpha_0$.

Several characteristic peaks of atmospheric absorption are available if hyperspectral data are processed in a wide wavelength range (e.g., 0.4–2.0 μm). Based on an analysis of these peaks, we can more accurately pass from brightness codes to SR physical values.

Figure 5a and 5b present SCs for dense vegetation and open soil, respectively before atmospheric correction (dot-and-dash line), after correction according to the multiplicative model (dotted line), and after correction according to the multiplicative–additive model (solid line).

Figure 5 indicates that the correction of atmospheric distortions according to the multiplicative and multiplicative–additive models generally gives similar results; however, we should note that the multiplicative additive model behaves slightly more correctly in the blue spectral region (channels 1–10), which is expressed in the absence of dense vegetation SC slope in this spectral region (Fig. 5a). A disadvantage of the multiplicative–additive model consists in that local distortions are present on the image since dispersion is estimated inaccurately and the image column brightness is average.

Three facts were established during the experimental studies. First, the above assumption that atmospheric parameters are constant along columns was completely confirmed. Second, it was indicated that analytical model characteristic points can theoretically be used to reduce the statistical correction data into the physical system of values. Third, it was revealed that analytical models of the atmospheric radiation transfer can be used (using the model developed at the Institute of Physics of the Atmosphere, Russian Academy of Sciences as an example) if the metrological parameters are determined very accurately during imaging, and the smallest errors in these parameters result in a substantial decrease in the atmospheric correction effectiveness, which is observed as HF SC distortions. The statistical atmospheric correction is largely free of this disadvantage.

HYPERSPECTRAL INFORMATION COMPLEXING

In different spectral channels, objects can be represented differently: they can be lighter in some channels and darker than surrounding objects in other channels. In this case the discernibility of objects varies in different channels. In a traditional approach to the combination of channels via averaging, individual objects substantially lose contrast with respect to the channels where they are most distinct. The problem of formation of one or several images, where all observed scene objects are represented very accurately, is stated. Such a problem statement has theoretical backgrounds (Eremeev et al., 2012).

Assume that we have a hyperspectral sensor with K spectral channels and a panchromatic sensor that operates in the same wavelength range. Two brightness vectors $\mathbf{B_1} = \left(B_{11}, B_{12}, \ldots, B_{1K}\right)$ and $\mathbf{B_2} =$

$(B_{21}, B_{22}, \ldots, B_{2K})$ will be formed when a hyperspectral sensor is used to image two points of the Earth's surface. Two brightness values $B_1 = \frac{1}{K}\sum_{k=1}^{K} B_{1k}$ and $B_2 = \frac{1}{K}\sum_{k=1}^{K} B_{2k}$ when a panchromatic sensor is used to image the same points. We consider the measures of discernibility of these points on panchromatic and hyperspectral images. For a panchromatic image, we accept the following parameter as a measure of discernibility of two points:

$$\ell = |B_1 - B_2| = \frac{1}{K}\left|\sum_{k=1}^{K}(B_{1k} - B_{2k})\right| = \frac{1}{K}\left|\sum_{k=1}^{K}\Delta B_k\right|.$$

For a hyperspectral image, as a measure of discernibility it is natural to accept the distance between two points in the spectral zonal space, having normalized this measure so that the variation range would coincide with measure ℓ:

$$d = \frac{1}{\sqrt{K}}\sqrt{\sum_{k=1}^{K}(B_{1k} - B_{2k})^2} = \frac{1}{\sqrt{K}}\sqrt{\sum_{k=1}^{K}\Delta B_k^2}.$$

We consider the ratio of these two measures:

$$\gamma = \frac{\ell}{d} = \frac{1}{\sqrt{K}}\left|\sum_{k=1}^{K}\Delta B_k\right| \Bigg/ \sqrt{\sum_{k=1}^{K}\Delta B_k^2}.$$

Hyperspectral imaging does not give additional information in order to improve the image resolution only at $x_1 = x_2 = \ldots = x_s$: $\gamma = 1$. The best conditions for integrating hyperspectral data are created as spectral zonal components neutralize one another $(\ell \to 0)$.

Several algorithms for integrating multispectral images based on some principles were proposed (Eremeev, 2012a; Eremeev et al., 2012). We consider the algorithm based on the polynomial representation of SCs and on an analysis of the polynomial relative position and average brightness level. For example, three variants are possible when SC is approximated by a polynomial of order 3: a polynomial crosses the average level ($\overline{B}$) at one, two, and three points. Parameter γ is correspondingly calculated for these cases.

In the first case the measure describing the SC variation character is defined as

$$\gamma = \begin{cases} -\sqrt{|(S_1 \cdot S_2)/(n_1 \cdot n_2)|}, & S_1 < 0; \\ \sqrt{|(S_1 \cdot S_2)/(n_1 \cdot n_2)|}, & S_1 > 0, \end{cases}$$

where $S_1 = \sum_{k=0}^{k_1}(B_k - \overline{B})$, k_1 is the number of the channel where a polynomial crosses the average brightness level, B_k is the brightness of SC approximated by a polynomial in channel k, $\overline{B}$ is the SC average brightness level of initial HIS, $S_2 = \sum_{k=k_1}^{K}(B_k - \overline{B})$, and $n_1 = k_1$, $n_2 = K - k_1$. If a polynomial and the average brightness level intersect at two points,

$$\gamma = \begin{cases} -\sqrt[3]{|(S_1 \cdot S_2 \cdot S_3)/(n_1 \cdot n_2 \cdot n_3)|}, & S_1 < 0; \\ \sqrt[3]{|(S_1 \cdot S_2 \cdot S_3)/(n_1 \cdot n_2 \cdot n_3)|}, & S_1 > 0, \end{cases}$$

where $S_2 = \sum_{k=k_1}^{k_2}(B_k - \overline{B})$, k_2 is the second point where a polynomial crosses the $\overline{B}$ level, $S_3 = \sum_{k=k_2}^{K}(B_k - \overline{B})$, $n_1 = k_1$, $n_2 = k_2 - k_1$, and $n_3 = K - k_2$. When a polynomial crosses level $\overline{B}$ at three points,

$$\gamma = \begin{cases} -\sqrt[4]{|(S_1 \cdot S_2 \cdot S_3 \cdot S_4)/(n_1 \cdot n_2 \cdot n_3 \cdot n_4)|}, & S_1 < 0; \\ \sqrt[4]{|(S_1 \cdot S_2 \cdot S_3 \cdot S_4)/(n_1 \cdot n_2 \cdot n_3 \cdot n_4)|}, & S_1 > 0, \end{cases}$$

where $S_1 = \sum_{k=0}^{k_1}(B_k - \overline{B})$, $S_2 = \sum_{k=k_1}^{k_2}(B_k - \overline{B})$, $S_3 = \sum_{k=k_3}^{K}(B_k - \overline{B})$, $n_1 = k_1$, $n_2 = k_2 - k_1$, $n_3 = k_3 - k_2$, and $n_4 = K - k_3$.

The B^* integration result is formed as $B^* = \overline{B} + \gamma$.

Figure 6a presents the image obtained as a result of averaging all HSI spectral channels from the ProSpecTir-V aviation sensor (USA); Fig. 6b shows the result of integration according to the described algorithm.

The synchronous panchromatic and (or) spectral zonal imaging of the Earth with a multiply higher spatial resolution (degree of detail) are usually performed when HSI is formed. It is necessary to integrate video information with a high spectral resolution with the data of very detailed imaging the Earth in order to obtain HSI with high spectral and spatial resolutions.

We consider one of the algorithms for solving this problem (Akhmetov and Stratilatov, 2011; Eremeev, 2012a, 2012b). Assume that $B \in \left\{B_{mnk}, k = \overline{1,K}\right\}$ HSIs and the $D \in \left\{D_{rsi}, i = \overline{1,I}\right\}$ spectral zonal image were obtained for the same scene; in this case the repetition periods of nodes (m, n) and (r, s) strongly differ; i.e., $R/M \gg 1$, $S/N \gg 1$. The algorithm for integrating B and D is based on the modulation of spectral components B_k by images D_i:

$$B^*_{rsk} = \frac{D_{rsi} \cdot B_{rsk}}{\overline{D_i B_k}} \cdot \overline{B}_k, \quad i = 1 + ent\left(k\frac{I}{K}\right),$$

where B^*_{rsk} is the kth component of resultant HSI, $B^* \in \left\{B^*_{rsk}, k = \overline{1,K}\right\}$, $\overline{D_i B_k} = \frac{1}{RS}\sum_{r=1}^{R}\sum_{s=1}^{S} D_{rsi} B_{rsk}$, $\overline{B}_k = \frac{1}{MN}\sum_{m=1}^{M}\sum_{n=1}^{N} B_{mnk}$, $B_{rsk} = \Phi(B_{mnk})$ is the HSI kth component reconstructed at dense grid nodes (r,s) by operator Φ.

Figure 7 presents the result of the HSI B and multizone image D integration as image B^*.

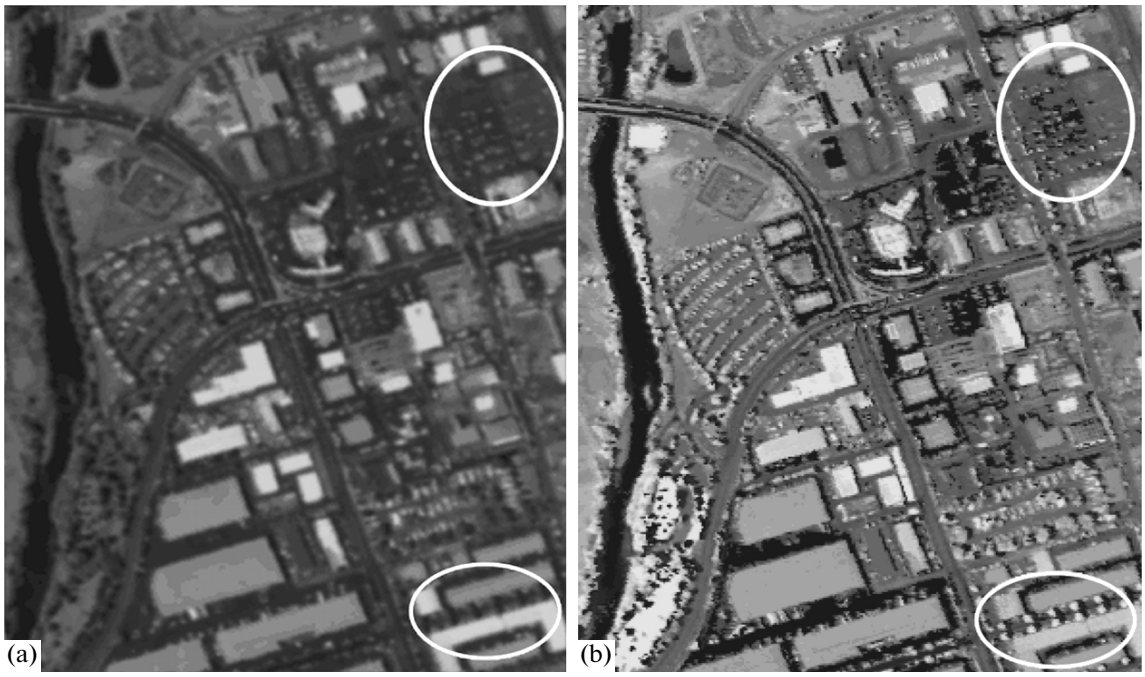

Fig. 6. Results of aviation hyperspectral image processing: (a) averaging of all HSI spectral channels, (b) integration.

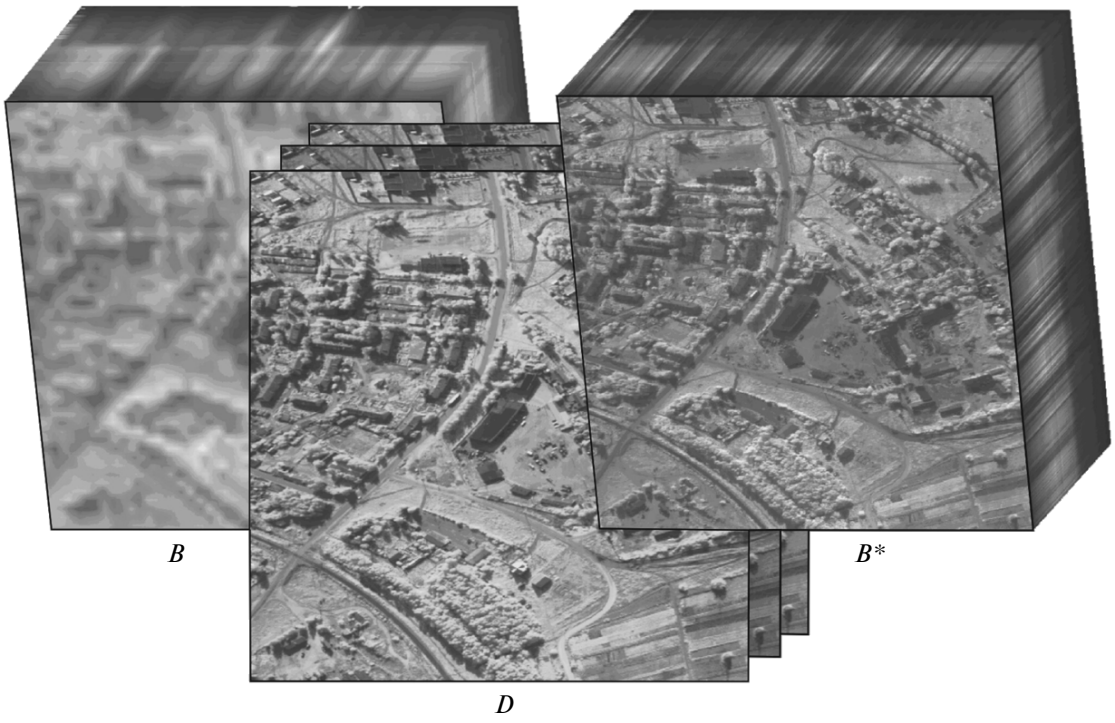

Fig. 7. Result of *B* integration with *D*.

The SC reconstruction accuracy was experimentally studied at points (r, s) that do not coincide with nodes (m, n). For this purpose, HSI with a low spatial resolution $\tilde{B}$ and image D were modulated. $\tilde{B} \in \left\{\tilde{B}_{mnk}, k = \overline{1, K}\right\}$ and $D \in \left\{D_{rsi}, i = \overline{1, I}\right\}$ were formed from initial HSI $B \in \left\{B_{rsk}, k = \overline{1, K}\right\}$ by rarefying readings by factors of 5, 10, 20, and 30 and by averaging the B_{rsk} components over corresponding spectral ranges $i = \overline{1, I}$. Then, we compared $B \in \left\{B_{rsk}, k = \overline{1, K}\right\}$ with the integration result $B^* \in \left\{B^*_{rsk}, k = \overline{1, K}\right\}$:

$$E = \frac{1}{KRS}\sum_{r=1}^{R}\sum_{s=1}^{S}\sum_{k=1}^{K}\left(\left|B_{krs} - B^*_{rsk}\right|\Big/B_{rsk}\right).$$

The following values were obtained at $K = 105$ and $\mu = 10$: when integration was performed with the single-zone (panchromatic) image ($I = 1$): $E = 1.1124\%$; during the integration with the three-zone image ($I = 3$): $E = 0.9128\%$. The dependence of the error value (E) on μ was analyzed. At $\mu = 5$, 10, 20, and 30, $E = 0.68$, 0.91, 1.16, and 1.27%, respectively.

CONCLUSIONS

We considered the HSI formation models, measures of image element similarity, new possibilities of image contour processing, a decrease in the HSI dimensionality, atmospheric distortion statistical correction, and integration of hyperspectral information with the data from other imaging systems. The studies in these directions were performed in the scope of the Resurs-P space system (FGUP GNP RKTs TsSKB-Progress, Samara, a leading developer). The algorithms considered in this work have been reduced to software complexes. They passed all types of tests, and were installed at the exploiting organization the Scientific Center for the Earth Online Monitoring, the Russian Space System corporation, Moscow. The main scientific results of the performed studies are as follows:

(1) We studied several measures of similarity between different hypercube elements based on comparing these measures with SC. We analyzed the effect of additive multiplicative noise in different HSI channels on the quality of the measures of difference between its elements. We proposed a new measure of similarity between HSI elements noncritical to the noise effect.

(2) We studied different approaches to a decrease in the hyperspectral information volume without a substantial loss of the spectral resolution. Specifically, we considered the polynomial algorithm for representing SC. We indicated that this algorithm makes it possible to reach an almost fourfold decrease in the calculations and a multiple decrease in the hyperspectral information volume without a substantial loss of the clustering and HSI contour processing quality.

(3) We proposed an atmospheric distortion statistical correction model based on a direct analysis of HSI. In contrast to the analytical multifactor atmospheric models, statistical correction makes it possible to substantially increase the HSI contour processing, clustering, and classification quality.

(4) We considered several HSI integration technologies: both hypercube channels and HSI integration with information from other imaging systems. Using the data from the ProSpecTir-V aviation system, we indicated that the usage of such technologies makes it possible to substantially improve the object resolution. The integration of hyperspectral resolution with a low spatial resolution with information from other imaging systems with a much higher resolution makes it possible to form a new hypercube with high spatial and spectral resolutions.

ACKNOWLEDGMENTS

This work was supported by the Russian Foundation for Basic Research, OFI-M-2013 project no. 13-01-12014.

REFERENCES

Akhmetov, R.N. and Stratilatov, N.R., New technologies for the analysis and processing of the Earth's remote sensing data, *Aerokosmicheskii Kur'er*, 2011, no. 6, pp. 22–24.

Akhmetov, R.N., Stratilatov, N.R., Yudakov, A.A., Vezenov, V.I., and Eremeev, V.V., Main directions of research on the development of technologies for processing of data from hyperspectral surveying of the Earth, *Proc. of the Scientific and Technical Conf. "Hyperspectral Instrumentation and Technologies,"* Moscow: JSC "Krasnogorskii zavod im. S.A. Zvereva," 2013, pp. 23–24.

Akhmet'yanov, V.R., Nikolenko, A.A., and Terent'eva, V.V., Development of space hyperspectral instrumentation in foreign countries, *Proc. of the Scientific and Technical Conf. "Hyperspectral Instrumentation and Technologies,"* Moscow: JSC "Krasnogorskii zavod im. S.A. Zvereva," 2013, pp. 41–42.

Antonushkina, S.V., Eremeev, V.V., Makarenkov, A.A., and Moskvitin, A.E., Specific features of analysis and processing of data obtained from hyperspectral surveying of the Earth's surface, *Tsifrovaya Obrabotka Signalov*, 2010, no. 4, pp. 38–43.

Arkhipov, S.A., Lyakhov, A.Yu., and Tarasov, A.P., Activities of JSC "Krasnogorskii zavod im. S.A. Zvereva" on the development of hyperspectral remote sensing instruments, *Proc. of the Scientific and Technical Conf. "Hyperspectral Instrumentation and Technologies,"* Moscow: JSC "Krasnogorskii zavod im. S.A. Zvereva," 2013, pp. 25–30.

Bondur, V.G., Modern approaches to processing large hyperspectral and multispectral aerospace data flows,

Izv., Atmos. Ocean. Phys., 2014, vol. 50, no. 9, pp. 840–852.

Eremeev, V.V., Makarenkov, A.A., Moskvitin, A.E., and Yudakov, A.A., Improving the contrast of objects on data of hyperspectral surveying of the Earth's surface, *Tsifrovaya Obrabotka Signalov*, 2012, no. 3, pp. 35–40.

Eremeev, V.V., Modern activities on the analysis and enhancement of quality of space images of the Earth's surface, *Tsifrovaya Obrabotka Signalov*, 2012a, no. 1, pp. 38–44.

Eremeev, V.V., Current problems in the processing of the Earth's remote sensing data, *Radiotekhnika*, 2012b, no. 3, pp. 54–64.

Gut, N., Hypercpectral imaging, *Spectroscopy*, 1999, vol. 14, no. 3, pp. 28–42.

Khailov, M.N. and Zaichko, V.A., Hyperspectral surveying—the prospects of its use in solving social and economic problems, *Proc. of the Scientific and Technical Conf. "Hyperspectral Instrumentation and Technologies,"* Moscow: JSC "Krasnogorskii zavod im. S.A. Zvereva," 2013, pp. 10–11.

Kozoderov, V.V., Kondranin, T.V., Dmitriev, E.V., Kazantsev, O.Yu., Persev, I.V., and Shcherbakov, M.V., Processing of hyperspectral aerospace sounding data, *Issled. Zemli Kosmosa*, 2012, no. 5, pp. 3–11.

Mahiny, A.S. and Turner, B.J., A comparison of four common atmospheric correction methods, *Photogram. Eng. Remote Sens.*, 2007, vol. 73, pp. 361–368.

Makarenkov, A.A. and Yudakov, A.A., Statistical correction of atmospheric distortions in hyperspectral satellite images of the Earth's surface, *Proc. of the All-Russian Scientific and Practical Conference "Current Problems of Space-Rocket Instrumentation and Information Technologies,"* Moscow: JSC "Rossiiskie kosmicheskie sistemy," 2012, pp. 54–55.

Pozhar, V.E. and Pustovoit, V.I., Possibilities for creating new vision systems on the basis of acoustic and optical video spectrometers, *Radiotekh. Elektron.* (Moscow), 1996, vol. 41, no. 10, pp. 1272–1278.

San, B.T. and Suzen, M.L., Evaluation of different atmospheric correction algorithms for EO-1 Hyperion imagery, International Archives of the Photogrammetry, *Remote Sens. Spatial Inform. Sci.*, 2010, vol. 38, no. 8, pp. 392–397.

Shovengerdt, R.A., *Distantsionnoe zondirovanie. Modeli i metody obrabotki izobrazhenii* (Remote Sensing. Models and Methods of Image Processing), Moscow: Tekhnosfera, 2012.

Yuhas, R.H., Goetz, A.F.H., and Boardman, J.W., Discrimination among semiarid landscape endmembers using the spectral angle mapper (SAM) algorithm, *Summaries 3rd Annual JPL Airborne Geosci. Workshop*, JPL, 1992, vol. 1, no. 92-14, pp. 147–149.

Zlobin, V.K. and Eremeev, V.V., *Obrabotka aerokosmicheskikh izobrazhenii* (Aerospace Image Processing), Moscow: Fizmatlit, 2006.

Translated by Yu. Safronov